Supplementary Information: Variations in human saliva viscoelasticity affect aerosolization propensity

Mariana Rodríguez-Hakim, Linard Räz, and Jan Vermant

S1 Material properties and rheology of Saliva

S1.1 Surface tension

The time-dependent surface tension, $\sigma(t)$, is shown for all saliva samples in Fig. S1. σ_0 differs by at most 5 mN/m among all donors, corresponding to at most a 10% variability.

S1.2 Shear viscosity

Fig. S2 shows the shear rate dependency of the dynamic shear viscosity, $\mu(\dot{\gamma})$, for all saliva samples. μ_∞ differs by at most 1 mPa·s among all donors, corresponding to approximately a two-fold difference among all donors. However, differences in the solute contribution to the shear viscosity, where $\mu_\infty = \mu_\infty^{solute} + \mu_\infty^{solvent} = \mu_\infty^{solute} + 1$ mPa·s, differ by about a factor of three.

S1.3 Extensional rheology - CaBER data

Sample data for the extensional filament thinning experiments is shown in Fig. S3 for native and pre-sheared salivas A and E. The elastocapillary regime is fit to an exponential decay function, and the extensional relaxation time is calculated from the exponential.

S1.4 Shear rheology - amplitude sweeps

Amplitude sweeps at a frequency of 1Hz are shown for all saliva samples in Fig. S7.

S2 Impinging jet experiments

S2.1 Impinging jet experiments for salivas B and D

Sample images for the impinging jet experiments of the salivary sheets provided by donors B and D are provided in Fig. S4.

S2.2 Rim instabilities in fluid sheets

Time sequences of both rim fragmentation processes are shown in Fig. S5 and Fig. S6. Fig. S5 depicts a Rayleigh-Plateau process, whereby a portion of the rim thickens and a ligament buds out. Fig. S6 depicts what we believe to be a Rayleigh-Taylor instability, where a portion of the rim fragments and is ejected from the sheet, forming a long, thin filament.

S2.3 State diagrams for salivas B and D

State diagrams that depict the progression through all four stability regimes are presented in Fig. S8 for the individual salivas B and D and for a 40% glycerol-water solution as a function of We, Re, and De.

S3 Coil-stretch transition

Beyond the coil-stretch transition at $\dot{\epsilon}\lambda = 1/2$, where $\dot{\epsilon}$ is the extensional rate of strain of the polymer, a polymer coil becomes highly extended and spans a larger interaction volume where physical entanglements with neighboring polymer molecules can occur [1]. We conduct an order of magnitude analysis to determine whether the coil-stretch transition is exceeded during the impinging jet experiments.

We begin by adopting a definition of the rate of strain analogous to the one used in capillary thinning extensional rheology experiments, where

$$\dot{\epsilon}(t) = \frac{1}{x(t)} \frac{dx(t)}{dt}, \tag{1}$$

and $x(t)$ is end-to-end distance of a given polymer molecule under stretch. We assume that, as in Newtonian sheets, there is no azimuthal velocity component (i.e null vorticity), that the streamlines emanate radially outwards from the impinging jet location, and that the sheet velocity is everywhere uniform and equal to U [2–4]. Thus, each of the two ends of the polymer molecule travels along a different streamline, and the path of the streamlines diverges as the polymer molecule flows further downstream. If the streamlines are separated by an angle ψ, then $x(t) = \psi U t + x_0$ and $dx(t)/dt = \psi U$, where x_0 is the initial end-to-end distance of the unstretched polymer coil and

$$\dot{\epsilon}(t) = \frac{U}{Ut + x_0}. \tag{2}$$

We take $U \sim 1$ m/s and $x_0 \sim 10$ μm [5], such that $\epsilon(t = 0) \sim 10^5$ 1/s and $\epsilon(t = L/U) \sim 10^2$ 1/s (where $L \sim 10^{-2}$ m is the length of the sheet).

If $10^{-3} \lesssim \lambda \lesssim 10^{-1}$ s, then for the smallest $\lambda \sim 10^{-3}$ s, $0.1 \lesssim \dot{\epsilon}\lambda \lesssim 100$; thus, the polymer exceeds the coil stretch transition as it travels along the sheet.

References

[1] C. Clasen, J. P. Plog, W.-M. Kulicke, M. Owens, C. Macosko, L. E. Scriven, M. Verani and G. H. McKinley, *J. Rheol.*, 2006, **50**, 849–881.

[2] J. W. M. Bush and A. E. Hasha, *J. Fluid Mech.*, 2004, **511**, 285–310.

[3] N. Bremond and E. Villermaux, *J. Fluid Mech.*, 2006, **549**, 273–306.

[4] A. L. Yarin, *Free liquid jets and films: hydrodynamics and rheology*, Longman Group UK Limited, London, 1993.

[5] G. W. Hughes, C. Ridley, R. Collins, A. Roseman, R. Ford and D. J. Thornton, *Sci. Rep.*, 2019, **9**, 17350.

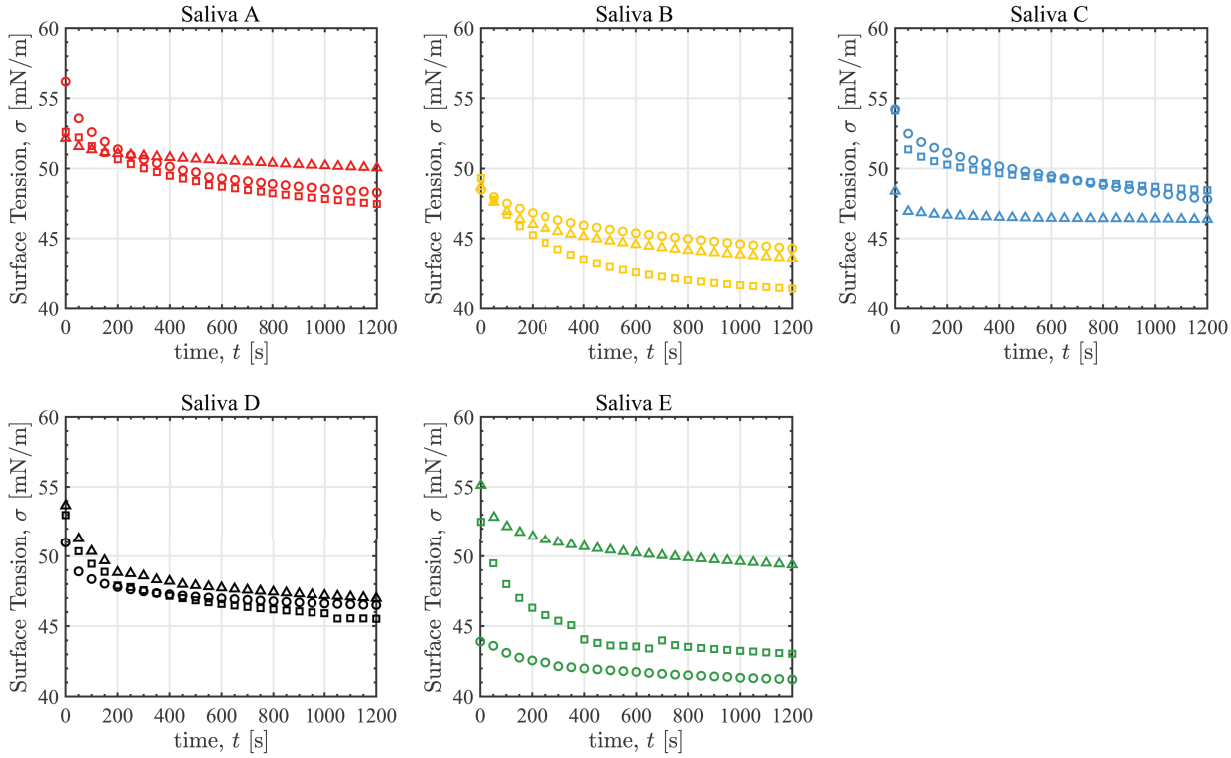

Figure S1: Time-dependent surface tension, $\sigma\,(t)$, for all saliva samples. Triplicate measurements on different days are conducted for each donor, such that three independent samples per donor are tested. The initial surface tension, $\sigma_0 = \sigma\,(t=0)$ is calculated from the measurement mean.

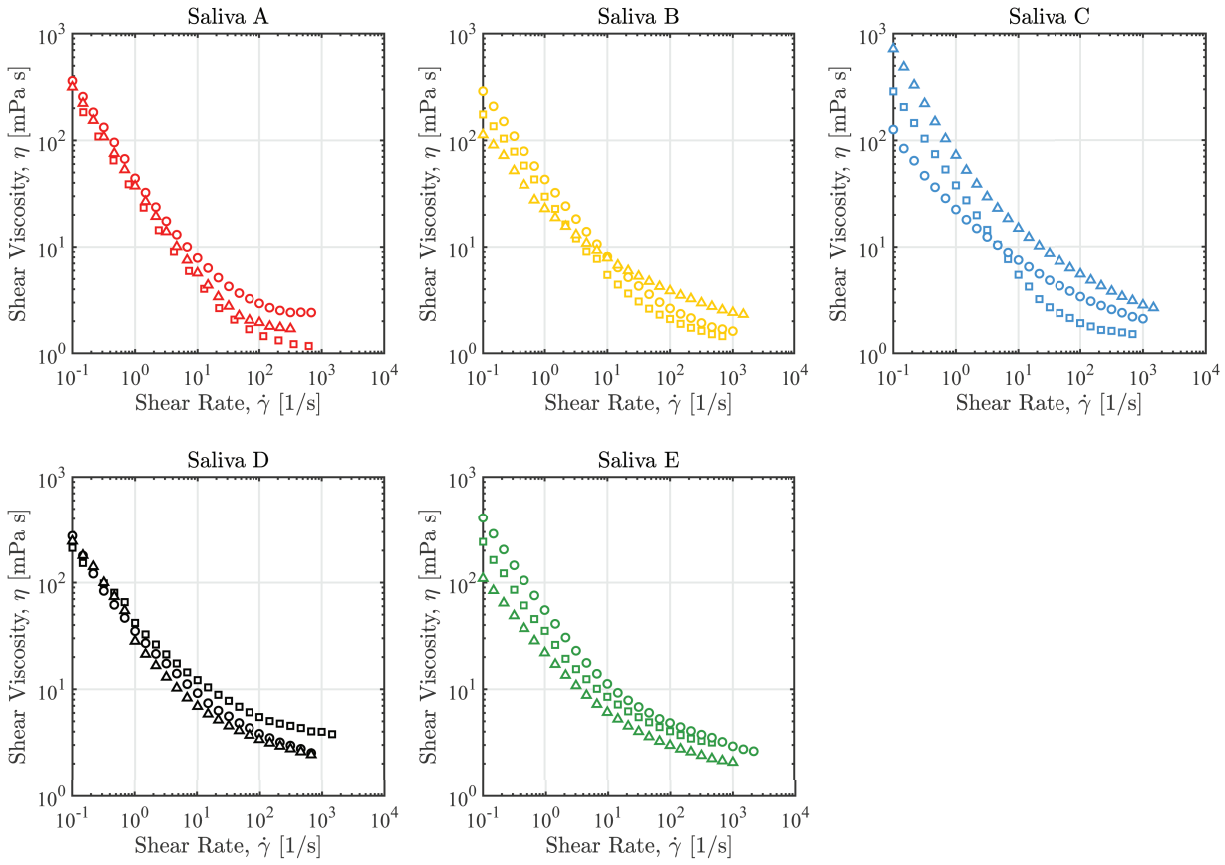

Figure S2: Shear rate-dependent dynamic viscosity, $\mu(\dot{\gamma})$, for all saliva samples. Triplicate measurements on different days are conducted for each donor, such that three independent samples per donor are tested. The infinite dynamic shear viscosity, $\mu(\dot{\gamma} \to \infty)$ is calculated from the Sisko model (see Materials and Methods section in manuscript) and the mean of all three measurements is taken.

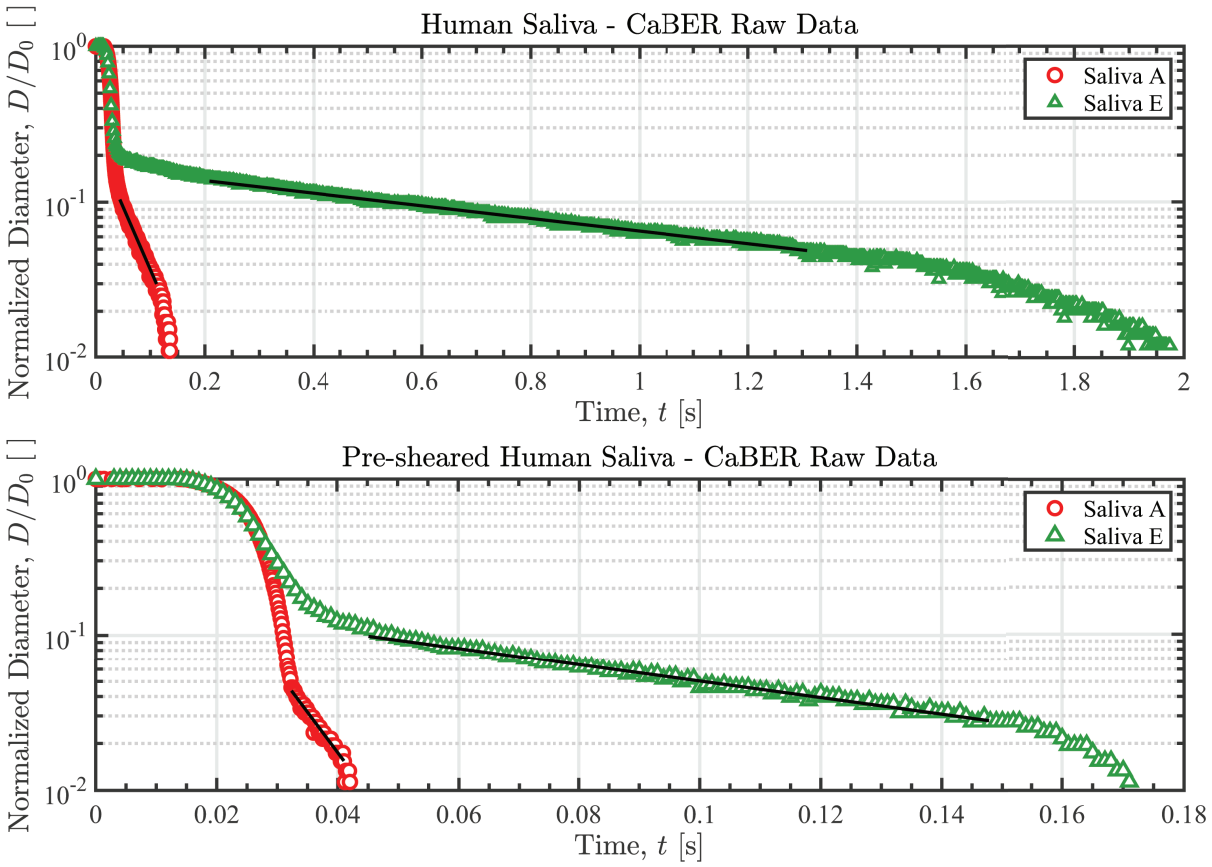

Figure S3: Sample raw data for the extensional capillary thinning (CaBER) experiments is shown for the native and pre-sheared saliva samples A and E. The plots show the normalized diameter, $D(t)/D_0$, as a function of time t. The elastocapillary regime is identified as the straight line region of the log-linear plot, as shown by the black lines. The data from the elastocapillary region is fitted to an exponential decay function. The extensional relaxation time is proportional to the exponential, where a less steep slope corresponds to a larger relaxation time (see the Materials and Methods section of the manuscript for the full expression).

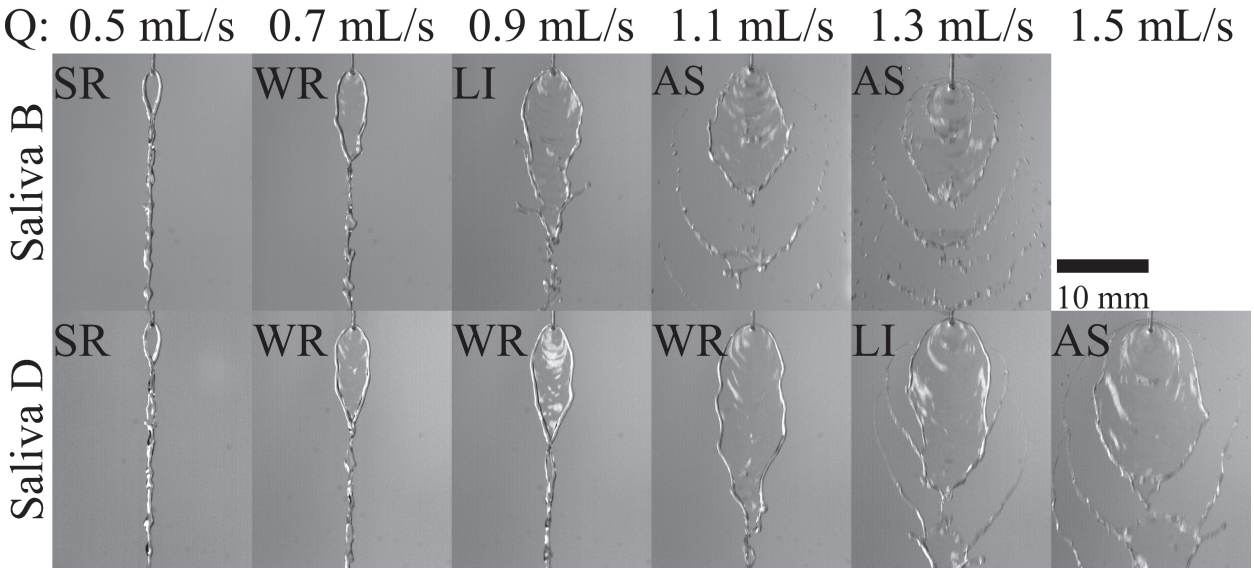

Figure S4: Impinging jet experiments of the salivary sheets provided by donors B and D. Each row represents the saliva provided by a different donor and columns represent the jet flow rates Q, where $Q = 0.5, 0.7, 0.9, 1.1, 1.3$, and 1.5 mL/s. A constant needle radius $R = 0.205$ mm is used for all experiments. Four regimes are used to classify the stability behavior of the sheets: SR (sheet with smooth rims), WR (sheet with wobbly rims), LI (ligament formation), and AS (atomizing spray).

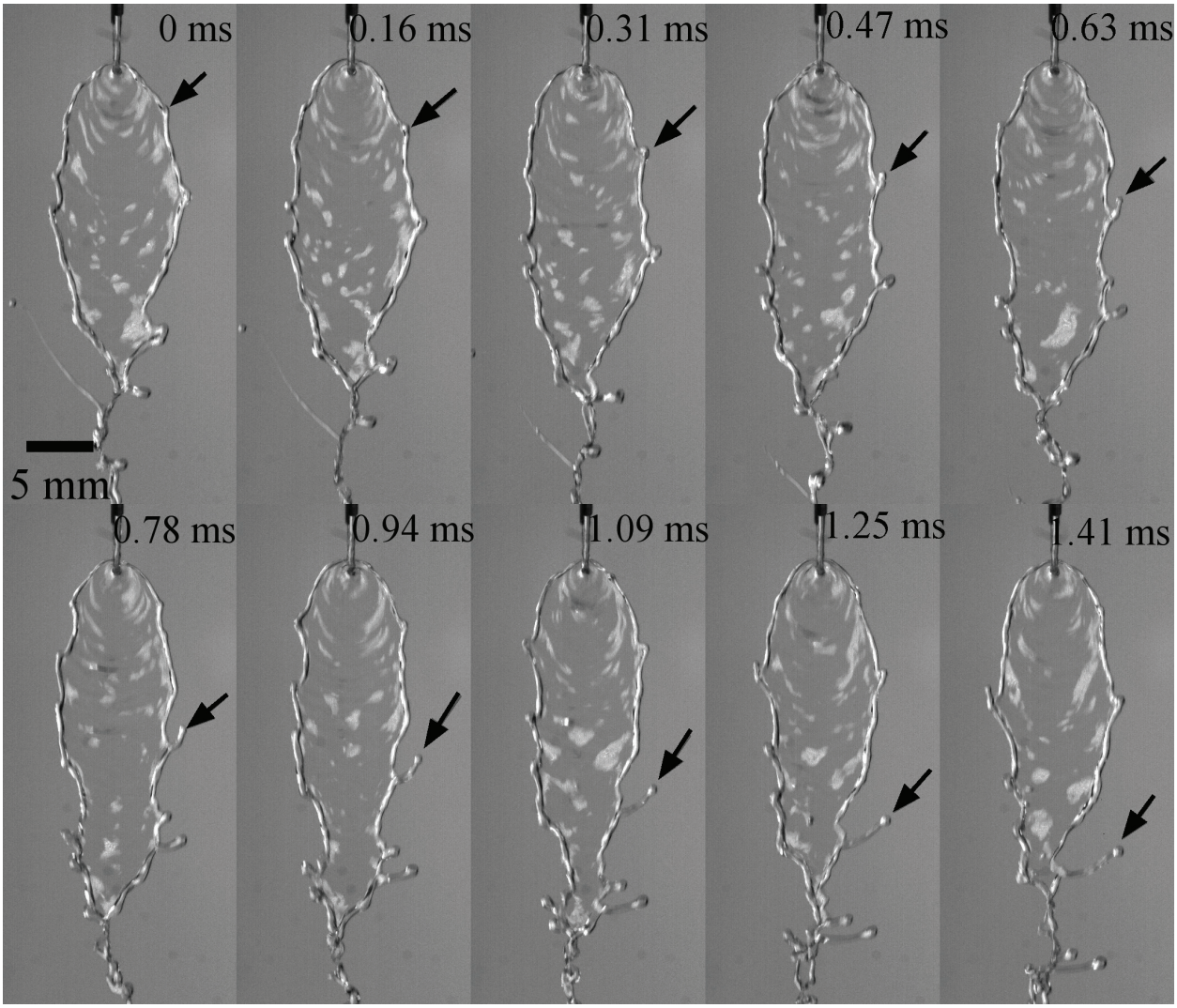

Figure S5: Image sequence of a Rayleigh-Plateau instability developing at the sheet's rim. A portion of the rim thickens and buds out into a ligament, which elongates as the fluid element flows towards the bottom of the sheet. Images correspond to Saliva A, with $R = 0.255$ m and $Q = 1.3$ mL/s.

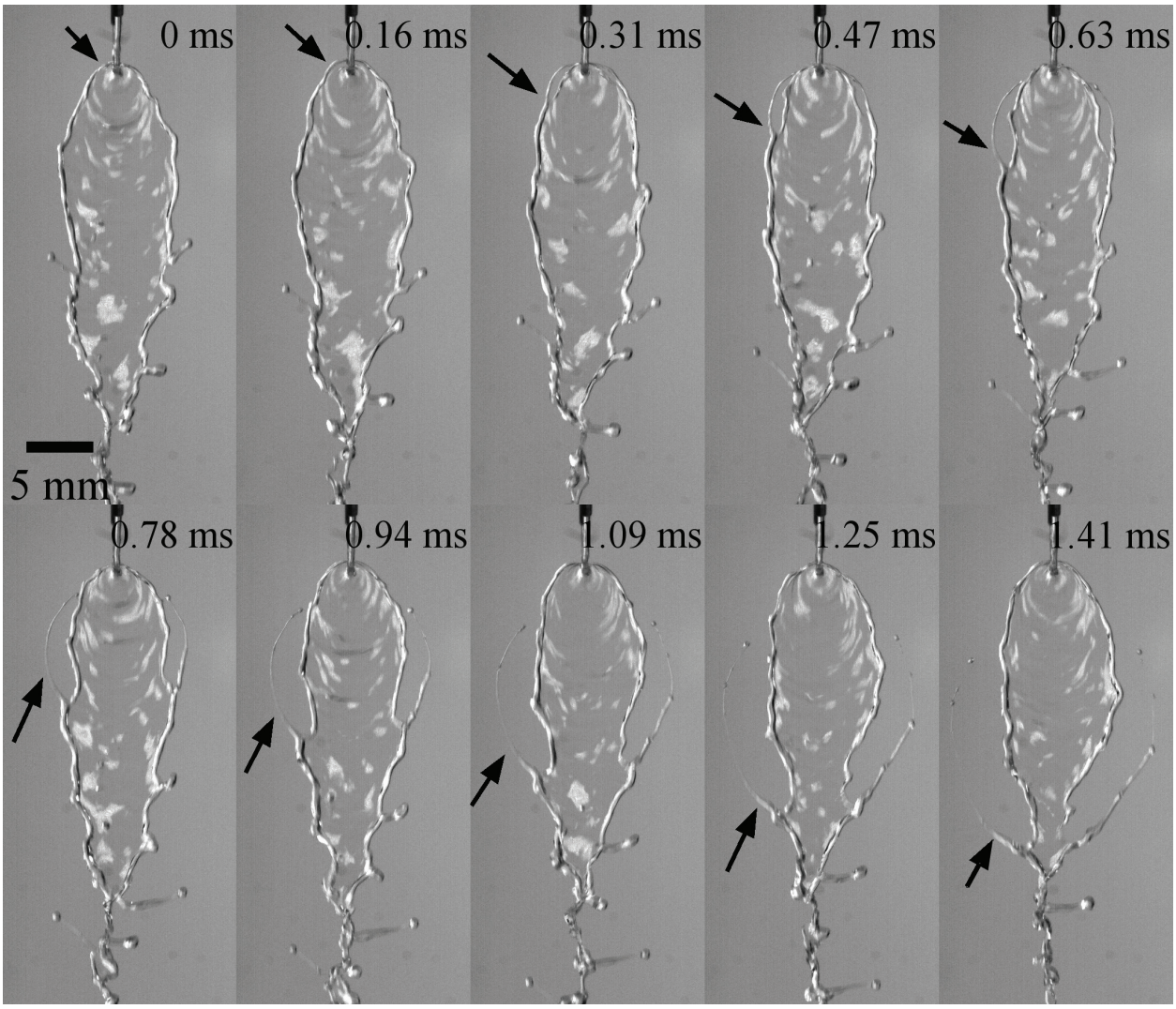

Figure S6: A second mode of instability was also observed, where the rim fragments and becomes discontinuous, and the downstream portion of the rim is ejected from the sheet as inertia deviates its path from its curved trajectory. This fragmentation process may be due to a centrifugally-forced Rayleigh-Taylor instability. Images correspond to Saliva A, with $R = 0.255$ m and $Q = 1.3$ mL/s.

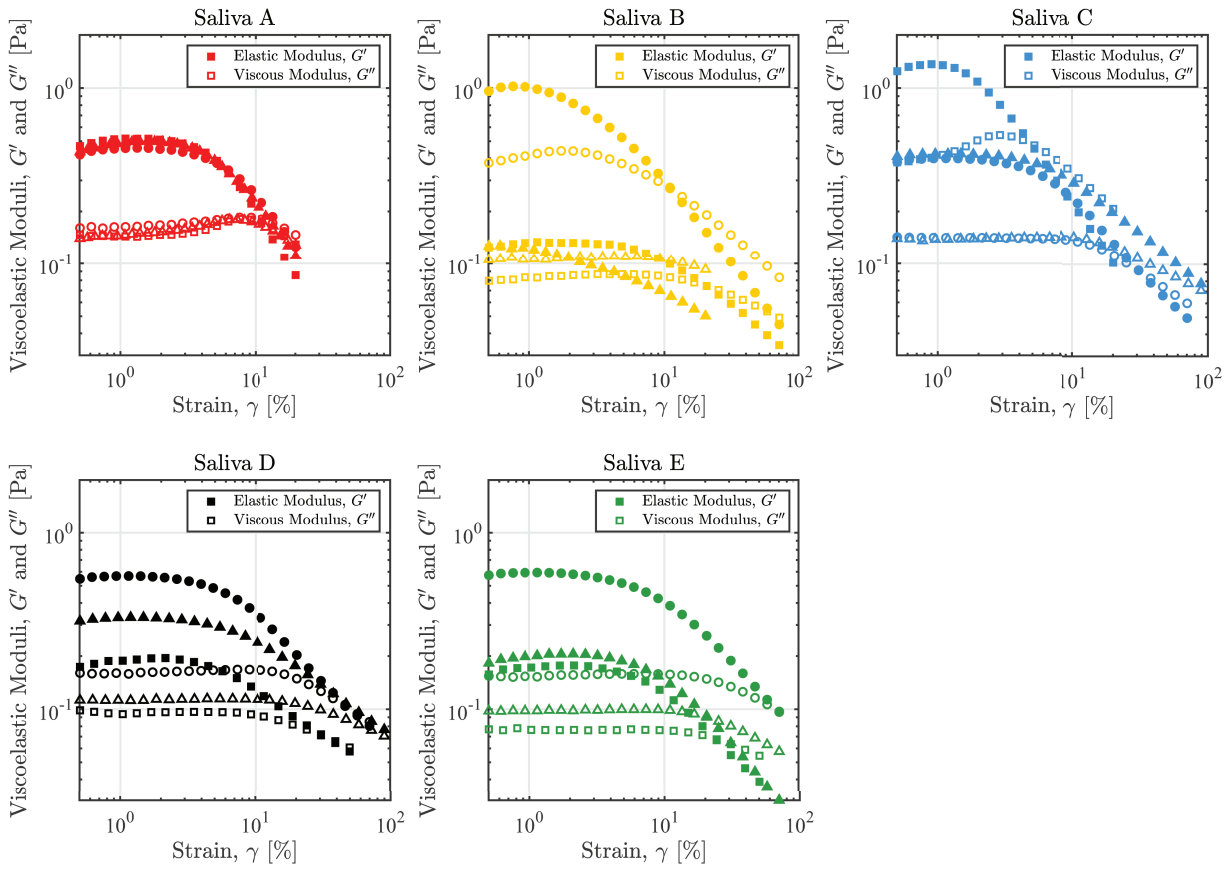

Figure S7: Small amplitude oscillatory shear rheology measurements of all saliva samples. Amplitude sweeps are conducted at a frequency of 1 Hz. The elastic modulus G', the viscous modulus G'', and the crossover strain γ_c, are calculated from the mean of three independent measurements per donor.

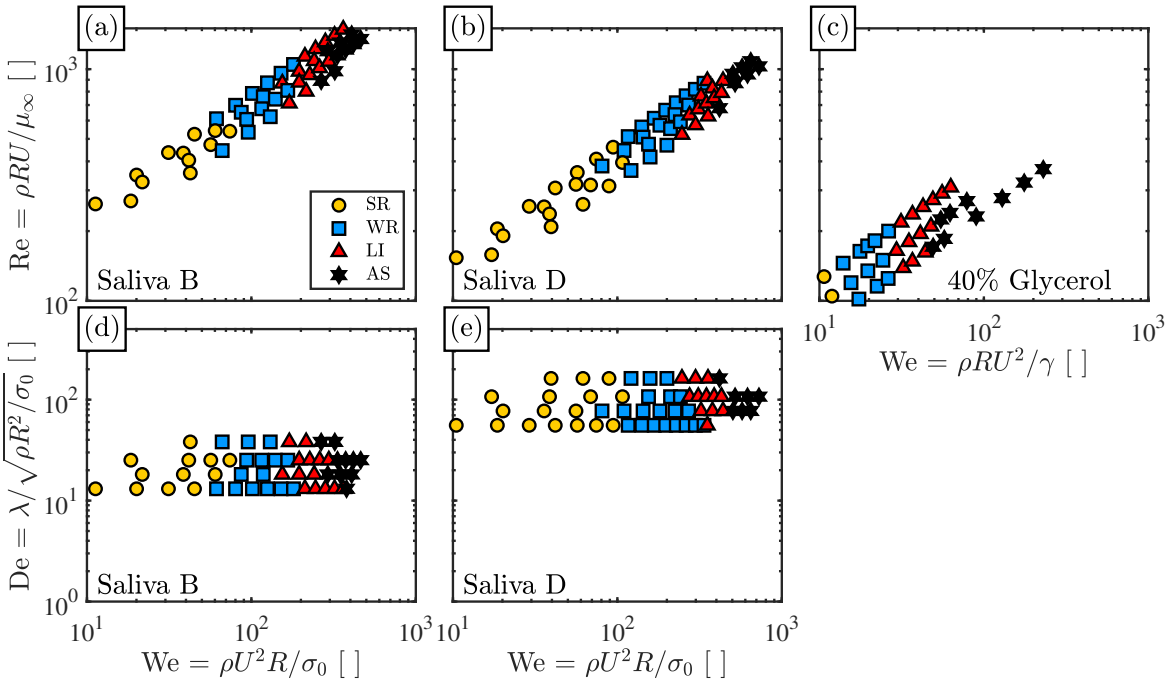

Figure S8: State diagrams for salivas B and D and for a 40% glycerol-water solution as a function of Re, We, and De. Although more viscous (as seen by the smaller Re), the Newtonain glycerol solution destabilizes and breaks up at lower values of We when compared to the elastic salivas. No De vs We diagram is shown for the Newtonian solution, since De=0.